Appl. Phys. A (2016)122:432
DOI 10.1007/s00339-016-9942-9

Applied Physics A
Materials Science & Processing

Laser-induced spalling of thin metal film from silica substrate followed by inflation of microbump

N. A. Inogamov[1] · **V. V. Zhakhovsky**[1,2] · **K. P. Migdal**[1,2]

Received: 18 October 2015 / Accepted: 28 February 2016

Abstract Dynamics of a thin gold film on a silica substrate triggered by fast heating with the use of a subpicosecond laser pulse is studied. The pressure waves generated by such heating may result in spalling (delamination) of the film and its flying away from the substrate after an acoustic time defined by the film thickness and speed of sound in metal. Intensity of the heating laser beam has the spatial Gaussian distribution in a cross section. Therefore, the heating of film surface is non-uniform along cylindrical radius measured from the beam axis. As a result of such heating, the velocity distribution in material flying away from the substrate has a maximum at the beam axis. Thus, the separated film has dome-like shape which inflates with time. Volume of an empty cavity between the separated film and the substrate increases during inflation. Typical flight velocities are in the range of 30–200 m/s. The inflation stage can last from few to several tens of nanoseconds if the diffraction-limited micron-sized laser focal spots are used. Capillary forces acting along the warped flying film decelerate the inflation of dome. Capillary deceleration of a bulging dome focuses mass flow along the dome shell in the direction of its axis. This results in formation of an axial jet and droplet in a tip of the dome. Our new simulation results and comparisons with experiments are presented. The results explain appearance of debris in a form of frozen droplets on a surface of an irradiated spot. This is the consequence of the capillary return of a droplet.

1 Introduction

It is known that laser ablation may leave a trace on a surface of a metal target in a form of a surface 3D nanostructures. These phenomena have a wide range of applications from microelectronics and nanoplasmonics to the laser-induced forward transfer printing (LIFT) and biology. There are periodic (ripples, see, e.g., [1–3]) or random structures; see experiments [4–7] and theory [7–9]. These periodic or random structures cover large irradiated areas over many wavelengths: $R_L \gg \lambda_{\text{opt}}$, here R_L is a radius of focal spot and $\lambda_{\text{opt}} \sim 1$ micron is an optical wavelength. Action of the extreme ultraviolet (EUV) or X-ray ultrashort pulse with much shorter wavelengths also may result in the random structures [9]. Here in this report, the small irradiated spots are considered in the case of single laser shot deposited in a *thin film on a substrate* [10–18], see Fig. 1. The film thickness d_f is assumed to be smaller than a heated depth in the corresponding bulk material after few picoseconds from energy deposition. The shapes of 3D bumps in this case of tight focusing are more controllable with increase in energy in contrast with the case of the larger area and random structures, see [13, 14]. The lateral (i.e., along a target surface) size of such small spots is comparable with an optical wavelength.

It is known that the random structures in the large spots $R_L \gg \lambda_{\text{opt}}$ appear, thanks to interplay between three ingredients: inertial expansion of matter, capillary deceleration, and freezing of molten material [8, 9]. As is shown

✉ N. A. Inogamov
nailinogamov@gmail.com

[1] Landau Institute for Theoretical Physics, Russian Academy of Sciences, Chernogolovka, Russian Federation

[2] Dukhov Research Institute of Automatics, ROSATOM, Moscow, Russian Federation

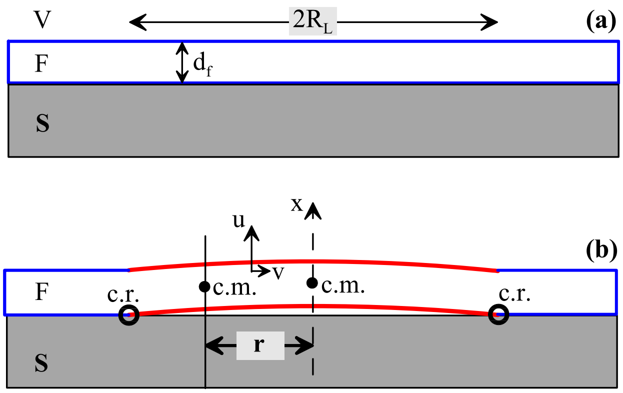

Fig. 1 Structure of our target: There is a thin film *F* with thickness d_f above the substrate *S*. Thus, the boundaries of a film are: the vacuum-film surface *V–F* and the film–substrate contact *F–S*. A diameter of the focal spot is $2R_L$. **a** Initial configuration. **b** Shortly after separation of a film from substrate inside the *circle* c.r. (contact ring). Here "shortly" means that the shift of the height of a dome tip Δh_c is small $\Delta h_c \ll R_L$ and that the capillary deceleration does not have time to decrease initial velocities $u_{\mathrm{cm}}(r)$ of vertical element of film at radius *r* after its separation from substrate

below, the same is true for the microbumps appearing in the case of the small spot $R_L \sim \lambda_{\mathrm{opt}}$. To demonstrate this, we extend the molecular dynamics (MD) simulations of dynamics of films presented in [18]. The extension includes electron heat conduction, thus describing resolidification of the gold films used in the experiments [10–14, 16, 19, 20]. The extension is based on a Monte Carlo (MC) module placed into MD–MPD3 code [21]). The combined version is called the MD–MC code.

There are two very different stages. A film separates from substrate during the first stage lasting $t_1 \sim t_s = d_f/c_s \sim 20$ ps, where t_s is an acoustic time required for propagating the film thickness with a sound speed c_s [18] (acoustic stage). After that, at the second (capillary/crystallization) stage, a film is mechanically and thermally linked to the substrate only outside the contact ring (c.r.) shown in Fig. 1b. Mach number $u_{\mathrm{cm}}(r)/c_s \sim 0.02$ of velocity of the center of mass (c.m.) of a film at a given cylindrical radius *r* is small in our cases. The ratio of durations of the second $t_2 \sim R_L/u_{\mathrm{cm}}(0)$ and the first stages is large $t_2/t_1 \sim [u_{\mathrm{cm}}(0)/c_s]^{-1} \times R_L/d_f \sim 10^3$ because both the Mach number and the relative thickness d_f/R_L of a film are small. Thus, the 20 ps for the first stage of sonic interference transfers into 20 ns for the second stage of capillary deceleration and freezing.

Separation of the two stages [18] greatly simplifies and makes more accurate the numerical solution of the problem. Classical MD method meets difficulties in applying at early electron-ion two-temperature stage, instead it is used at later stage. To describe the first short stage, the two-temperature hydrodynamics code (2T-HD) [18] including full two-temperature physics lasting $\sim$5–7 ps in gold is used. The 2T-HD modeling gives the distribution of electron–ion equilibrium temperatures $T(r)$ and velocities $u_{\mathrm{cm}}(r)$ along a film shown in Fig. 1b before detachment (delamination) of film. A moment of detachment was determined in 2T-HD via a stress criterion at the gold–glass contact, which triggers to start MD–MC simulation using those modeled distributions as initial data after film detachment. The contact adhesion strength between gold and glass is not well known, but it is <0.5 GPa. We varied the contact strength from 0 to 0.5 GPa and found that the detachment velocity is weakly dependent from the adhesion strength in the given range.

We run a series of the 2T-HD simulations for a set of absorbed fluences $F_{\mathrm{abs}}(r)$ belonging to a Gaussian distribution of absorbed fluences along a radius *r*. We neglect vertical (i.e., along *x*, see Fig. 1) variations of temperature $T(r, x, t_{\mathrm{sep}}) \approx T(r)$ because they become small at the instants of detachments $t_{\mathrm{sep}}(r)$. The characteristic heating length is about 120 nm in gold on two-temperature stage. Thus, the lateral heat flux during this early stage is negligible for micrometer-sized focal spot typical in experiments. However, the lateral thermal conductivity at later times plays a crucial role in freezing of the cupola and jets. Thus, we neglect lateral (along *r*) heat conduction during the 2T-HD simulations since the sonic stage is short and the smooth lateral temperature gradients cannot laterally redistribute absorbed energy during the sonic stage.

But at the long-lasting capillary/crystallization stage, the tangential (along a surface of a film) heat conduction is the only mechanism of cooling leading to crystallization and it, of course, is included into MD–MC simulation. Crystallization sharply suppresses fluidity of molten matter and qualitatively changes dynamics of motion.

Below, we drop out the descriptions of the first stage because they may be found in paper [18]. The parametric space of the considered problem with an ultrashort pulse and a thin film on substrate is presented in Sect. 2. After that, the two-dimensional and three-dimensional cases of a film blistering are considered in Sects. 3 and 4. In the 2D case, a laser irradiates a film through a slit [16, 18]. Therefore, the heated area has a form of a strip with a width $2R_L$ in Fig. 1. The strip is perpendicular to the plane of Fig. 1. In the 3D case, a laser beam has a cylindrical shape. In Sect. 4, the normal incidence is considered when a heated spot has an axial symmetry around the beam axis.

2 Main parameters

Let's consider the second stage. At this stage, the deceleration caused by a resistance of surface tension to stretching counteracts to an inertial inflation of a dome.

Without surface tension, the current shape of a dome $x(r,t) = u_{\mathrm{cm}}(r)t$ is defined by inertial motion (free flight). Here, we neglect lateral velocities $v_{\mathrm{cm}} \ll u_{\mathrm{cm}}$ at the instant of detachment because $d_f \ll R_L$, see Fig. 1. A capillary velocity scale

$$u_\sigma = 2\sqrt{\sigma/\mu} = 60\,[\mathrm{m/s}] \tag{1}$$

follows from energy balance

$$\rho\, d_f\, u_\sigma^2/2 = 2\sigma,$$

here σ is a coefficient of surface tension, $\mu = \rho d_f$ is areal mass density, ρ is density of a film, and the value $u_\sigma = 60\,\mathrm{m/s}$ corresponds to a gold film $d_f = 60\,\mathrm{nm}$ slightly above the melting temperature. It is remarkable that the scale (1) does not contain the radius R_L. We see that, an arbitrarily weak tension σ will stop inflation and will return a liquid film back onto a substrate. Indeed, kinetic energy per unit of mass is limited while surface energy increases proportionally to area of a stretched surface. This is true for an infinitely stretchable film. If we suppose that a film is homogeneously stretched $d \propto 1/x$ then vertical velocity u of a flying film loses a decrement of the order of u_σ (1) when a film lifts up one spatial scale R_L, see Fig. 1. This follows from conservation of mechanical energy. The homogeneous stretch means that the current local thickness d of a film is mainly the same along a flying film. Then, conservation of mass gives $d \propto 1/x$ in 2D and 3D where x is a current height of a dome above a substrate.

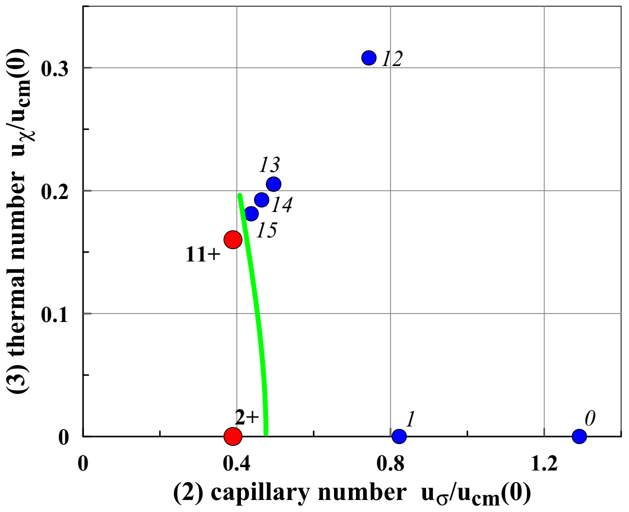

Fig. 2 The family of the 2D runs. The digits near the markers give the numbers of the runs presented in Table 1. The *green curve* separates the cases with no ejecta (the *blue circles*) and with ejecta (the *red circles*). The high-velocity cases have larger velocities $u_{\mathrm{cm}}(0)$ and are more close to the origin (0, 0). In the cases without ejecta, the surface tension is strong enough to return back all material separated from substrate. Transition between the cases with and without ejecta is rather sharp, compare the runs 14, 15 from the one side with the run 11+ from the other side. Here and in Table 1, the sign *plus* marks the cases with ejecta when a part of a metal film ablates away to infinity

Table 1 Simulation parameters for a family of the 2D runs, see text for definitions and Fig. 2

No.	$N_{\mathrm{atom}}/10^6$	L_b (nm)	d_f (nm)	(2)	(3)
0	3	440	27	1.3	0
1	1.1	620	7.4	0.82	0
2+	1.2	620	8.1	0.39	0
11+	0.86	140	5.1	0.39	0.16
12	0.86	140	5.1	0.74	0.31
13	0.86	140	5.1	0.5	0.21
14	0.86	140	5.1	0.46	0.19
15+	0.86	140	5.1	0.44	0.18

Capillarity strongly influences dynamics of stretching. It redistributes tangential mass flow, accumulating mass in the axial region of a flying dome. Then, there is faster stretching[1] outside the axial region and hence there is fast decrease in thickness while near the axis a thickness of a film begins to grow. Strength of surface tension is controlled by an important capillary parameter

$$u_\sigma/u_{\mathrm{cm}}(r=0), \tag{2}$$

here $u_{\mathrm{cm}}(0)$ is velocity in the tip immediately after separation of a film from a substrate. Large surface tension

$$u_\sigma/u_{\mathrm{cm}}(0) \gg 1$$

returns a separated film back onto substrate after small $x \ll R_L$ lifting x of a film above a substrate. If cooling and motion of a film both are slow then the Marangoni effect due to dependence $\sigma(T)$ can redistribute mass of a liquid film along a substrate. The Marangoni effect is insignificant in our conditions with a small spot (thus fast cooling and recrystallization), rapid motion, a metal film,[2] and a moderate temperature difference: $T(r=0) - T(r_{\mathrm{c.r.}})$ is of the order of or less than the melting temperature T_{m} (1337 K for gold), $r_{\mathrm{c.r.}}$ is radius of a contact ring, see Fig. 1b. Surface tension gradient

$$-\frac{T_{\mathrm{m}}}{\sigma(T_{\mathrm{m}})}\frac{\mathrm{d}\sigma}{\mathrm{d}T} = \frac{5}{4}\frac{T_{\mathrm{m}}/T_{\mathrm{cr}}}{1 - T_{\mathrm{m}}/T_{\mathrm{cr}}} = 0.25$$

is small because for metals the T_{m} is significantly less than the critical temperature T_{cr} (≈8000 K for gold). Therefore, in a flight, the dynamical role of surface tension itself is larger than the role of differences in σ along a film. Here, we use dependence $\sigma = \sigma_{\mathrm{m}}[(1 - T/T_{\mathrm{cr}})/(1 - T_{\mathrm{m}}/T_{\mathrm{cr}})]^{5/4}$ [18, 22] to calculate $\mathrm{d}\sigma/\mathrm{d}T$. In our MD simulations, we do

---

[1] In comparison with the case $\sigma = 0$ and purely inertial flow.

[2] Thus, the ratio of critical to melting temperature $T_{\mathrm{cr}}/T_{\mathrm{m}}$ is large.

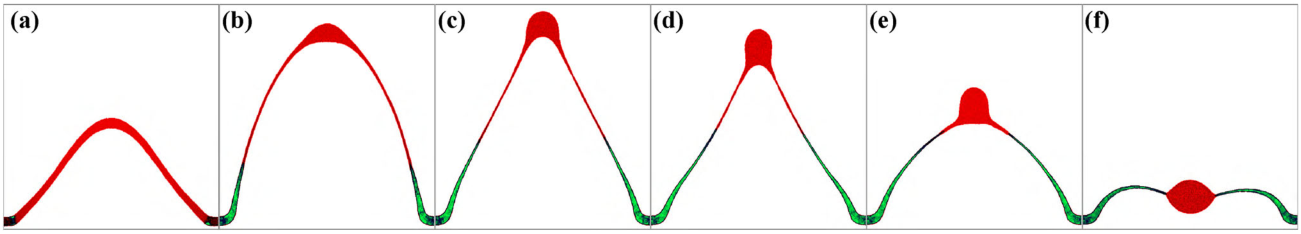

Fig. 3 The run 14 without ejecta. It is very close to the separation line in Fig. 2. Its “opponent” with ejecta is the run 11+ shown in Fig. 5. Difference between their parameters is rather small, see Table 1. Therefore, the inflation stages (**a–c**) of these two runs are rather similar. Colors give values of a symmetry parameter: *red* is liquid gold, *green* is solid. Thermal contact between a thin film forming a dome and the thickening is weak. Thus, the massive thickening for long times remains in liquid state. The vertical and horizontal scales are equal in all figures. The instants for the frames are: **a** 216 ps, **b** 648 ps, **c** 936 ps, **d** 1.15 ns, **e** 1.44 ns, **f** 1.73 ns

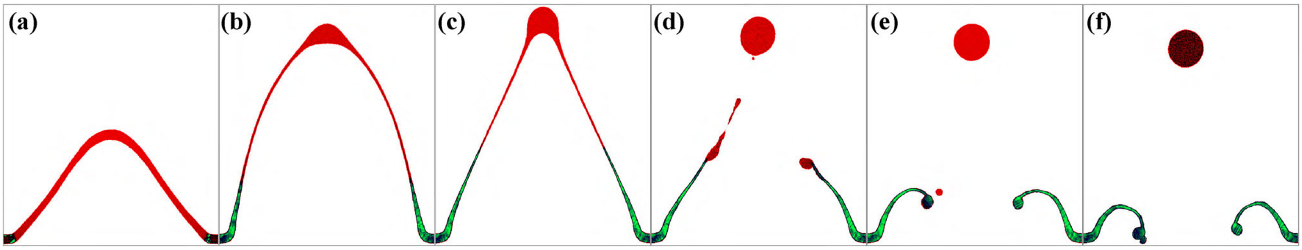

Fig. 4 The run 15 is also (as the case 14 in Fig. 3) without ejecta, but with separation of the thickening from the dome. Thus, the runs 14 and 15 are qualitatively different after finishing of the inflation stage. The thickening forms a large droplet accumulating significant part of mass contained inside the area between the points c.r. shown in Fig. 1b. The droplet slowly moves back to the substrate forming the debris in a form of the droplet inside the strip of the open silica substrate. The instants for the frames are the same as for Fig. 3

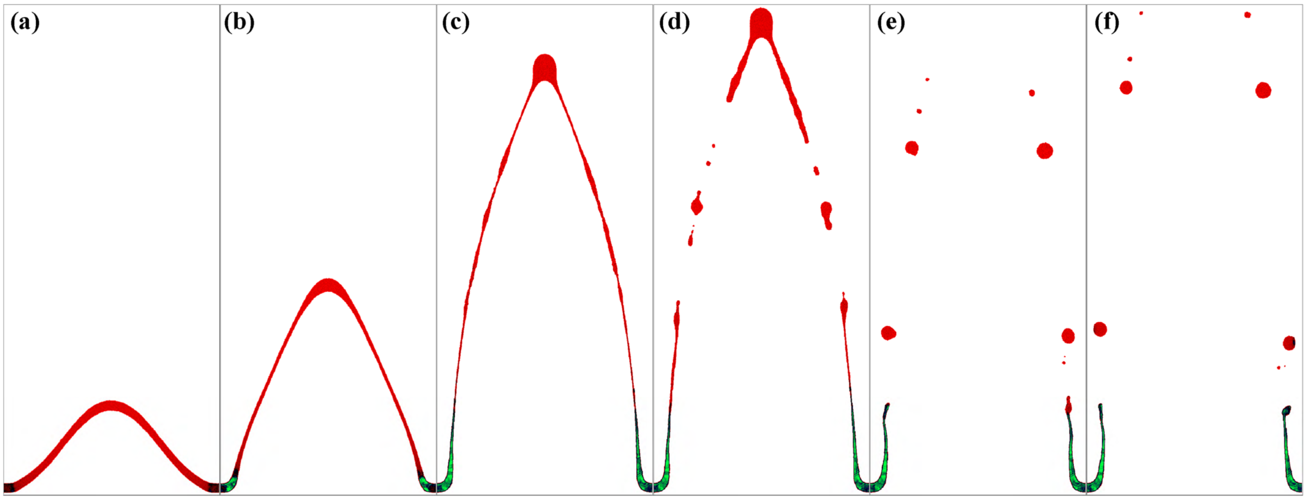

Fig. 5 The run 11+ with ejecta. The instants are: **a** 144 ps, **b** 360 ps, **c** 648 ps, **d** 720 ps, **e** 864 ps, **f** 1 ns. Let’s pay attention to the border structures near the ablation threshold. We see that they are different for the cases 15 and 11+. Such final structures are observed in all experiments [10–16, 18–20] with films. The open silica area inside the margin structures may be empty as here or may contain a droplet as in the case 15 shown in Fig. 4

not see any significant traces of the Marangoni effect. Surface tension coefficient of the interatomic potential [23] (used here in MD) depends on temperature [18].

In our applications [10–16, 18–20] velocities $u_{\mathrm{cm}}(0)$ are limited from above. Hence, the parameter (2) cannot be too small. The thickening in the tip of a flying dome begins to

Table 2 Simulation parameters for the 3D runs, see also Fig. 6

No.	$N_{\text{atom}}/10^6$	L_b (nm)	d_f (nm)	(2)	(3)
3+	192	620	8.3	0.39	0
20	6.0	140	5.1	0.39	0.16
21+	6.0	140	5.1	0.19	0.080
22+	6.0	140	5.1	0.10	0.040
23	6.0	140	5.1	0.39	0.32
25+	6.0	140	5.1	0.19	0.16
26+	2.1	140	1.8	0.16	0.080
27+	2.1	140	1.8	0.25	0.12
28+	6.0	140	5.1	0.10	0.080
30	44.	270	10	0.28	0.17
31+	44.	270	10	0.27	0.16

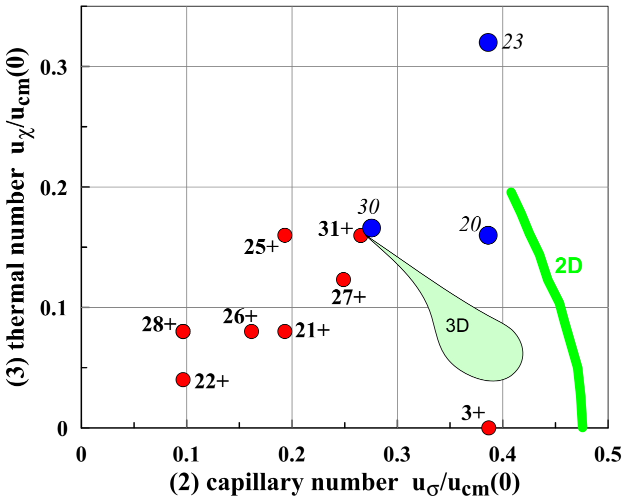

Fig. 6 The family of the 3D runs. The digits near the markers give the numbers of the runs presented in Table 2. The cases with (without) ejecta are *red* (*blue*). The region "3D" separates these cases. Transition from the case with ejecta to the case without ejecta is sharp, compare the runs 30 and 31+. Today is unknown where this transition takes place to the *left side* and to the *right side* from the runs 30 and 31+. Therefore, the transition region "3D" is plotted wider to the *right*. It separates the runs 3+ and 20. The transition/separation curve "2D" is taken from the plane of the parameters for the 2D geometry, see Fig. 2. For the same values of σ and μ, see (1), action of surface tension is stronger in the 3D geometry, thanks to additional dimension and radius of curvature. Thus, the "3D" curve is inside the "2D" curve

form for $u_\sigma/u_{\text{cm}}(0) \sim 1$ at the instants $t \sim R_L/u_{\text{cm}}(0)$. The evolution of the thickening is different in 2D and 3D. In our series of simulations, we do not see formation of a jet in the 2D case. Dependence on geometry is discussed in next sections.

Another important parameter is

$$u_\chi/u_{\text{cm}}(0), \quad u_\chi = \chi/R_L, \quad \chi = \kappa/c, \tag{3}$$

here κ is an electron heat conduction coefficient, c is a heat capacity, and χ is a heat diffusivity. The ratio (3) characterizes the relative rate of cooling. The cooling time R_L/u_χ is smaller if the spot size is smaller and diffusivity χ is larger.

3 Two-dimensional geometry

A family of the accumulated 2D runs is listed in Table 1 and in Fig. 2. Number of atoms N_{atom} is given in the second column of Table 1. The horizontal dimension of the computational box is L_b. A film separates from a substrate in a slit $2R_L$ shown in Fig. 1. There are two pieces of a film $L_b/2 - R_L = 5 - 10\,\text{nm}$. They are the left and right margins with fixed positions. A film at these margins remains attached to the substrate, thanks to action of the Langevin thermostat maintaining zero mass velocity in these parts of film, see Figs. 3, 4 and 5. Thus, a directed up initial vertical momentum of film, see Fig. 1, gradually decreases due to the surface tension and the mechanical link to the margins. For the runs Nos. 0–3 with $\kappa = 0$ (no electron thermal conductivity, pure MD runs—without the MC module), from Tables 1 and 2, the initial temperature distribution is homogeneous with $T = 1600\,\text{K}$. For MD–MC simulation with electron thermal conductivity, the initial central temperature $T(r=0, t=0) = 2000\,\text{K}$ in all other 2D and 3D runs is listed in Tables 1 (2D) and 2 (3D). The initial temperature profile decreases smoothly from the center $r =$ 0 to the margins $r_{\text{cr}} < r < L_b/2$. The thermostat prepares the thermalized molten initial state with temperature of the margins 1500 K above melting temperature of gold. After beginning of the MD–MC simulation with heat conduction, the thermostat was switched off everywhere except the margins. In the margins, the thermostat gradually decreases the supporting temperature from 1500 to 500 K during a few picoseconds. Thermal flux along a film from the central region to the margins simulates a cooling flux from the hot spot to the external cold area of a film. Values of the parameters (2) and (3) for the 2D case are presented in the last two columns of Table 1. They also are shown in Fig. 2. As was said, these parameters characterize surface tension and heat conduction.

Capillary forces have vertical and horizontal components; in Fig. 1, the vertical direction is x. The vertical component decelerates expansion of a dome and decreases initial velocity $u_{\text{cm}}(0)$, while the horizontal component accelerates fluid particles in a flying film toward the axial region thus forming the thickening in the central region of a dome. This is shown in Figs. 3, 4 and 5. The thickening accumulates significant part of moving mass and significant part of the current value of a vertical momentum. Inertia of the thickening is large, and it is difficult to decelerate it by the capillary forces. There is a strong stretching of a film during

Fig. 7 Local atomic order parameter mapped in the final cross section of axial-symmetric solid bump for the non-ejecting run 30 is listed in Table 2 and Fig. 6. This view is often met in experiments at the intermediate pulse energies, see, e.g., [14] or Fig. No. 3 in [26]. Let us pay attention to the grains of the nanocrystallites forming the bulged shell. The *dark lines* show lattice defects such as dislocations or boundaries between grains. The horizontal size of cross section is $L_b = 270\,\mathrm{nm}$

action of surface tension against the breaking out of the thickening. The stretching greatly decreases thickness of a film in the piece of a film between the crystallization front and the thickening, see Figs. 3 and 4.

If a film survives unbroken up to the reversal of motion of the thickening from the out direction to the back to the substrate direction, then, after the reversal, the thickness of the liquid part of the film begins to grow. This case, corresponding to the run 14 in Table 1 and Fig. 2, is shown in Fig. 3. There is no ejecta in the case when the thickening turns back. All separated mass returns back to a substrate forming a frozen microbump. Thickness of the returned film is inhomogeneous. There is a thinner film around the thickening (droplet) in the central zone. This is a result of stretching and freezing of the film in fly. Final strong thinning of a frozen film as in Fig. 3f recently has been observed experimentally [24].

The green curve in Fig. 2 divides the cases when there is an ejecta at infinity from the cases when all matter of a film remains in contact with a substrate. The runs without (with) ejecta are marked with the blue (red) circles in Fig. 2. The runs 14 and 15 described above belong to the case without an ejecta: Capillarity overcomes kinetic energy of expansion. But small increase (see Table 1 and Fig. 2) in kinetic energy from the runs 14, 15 to the run 11+ does impossible to keep the central thickening in mechanical contact with the substrate up to the instant of the reversal. While at the inflation stage of a dome, lasting up to the instant ≈700–900 ps, the runs 14, 15, and 11+ are close to each other.

The run 14 in Fig. 3 and the run 15 in Fig. 4 both do not produce ejecta and, as was said, are very similar at the inflation stage (a–c). This is not surprising because their parameters are close, see Table 1. Surprising is the another thing. Even these tiny difference in the parameters produces the sharp qualitative change of the final structures—compare Fig. 3f with the integral bump and Fig. 4f with the broken bump made from the margin walls and the droplet at the surface of the silica substrate. There are many experimental pictures showing existence of the debris in and around the irradiated spot, see. e.g., Fig. No. 6 in [25] and papers [14, 26]. Sometimes people surprise, how the debris may appear? Indeed, the ablated matter flies out into the vacuum side, and there is no any obstacle ahead which can reflect ejecta back. Our simple

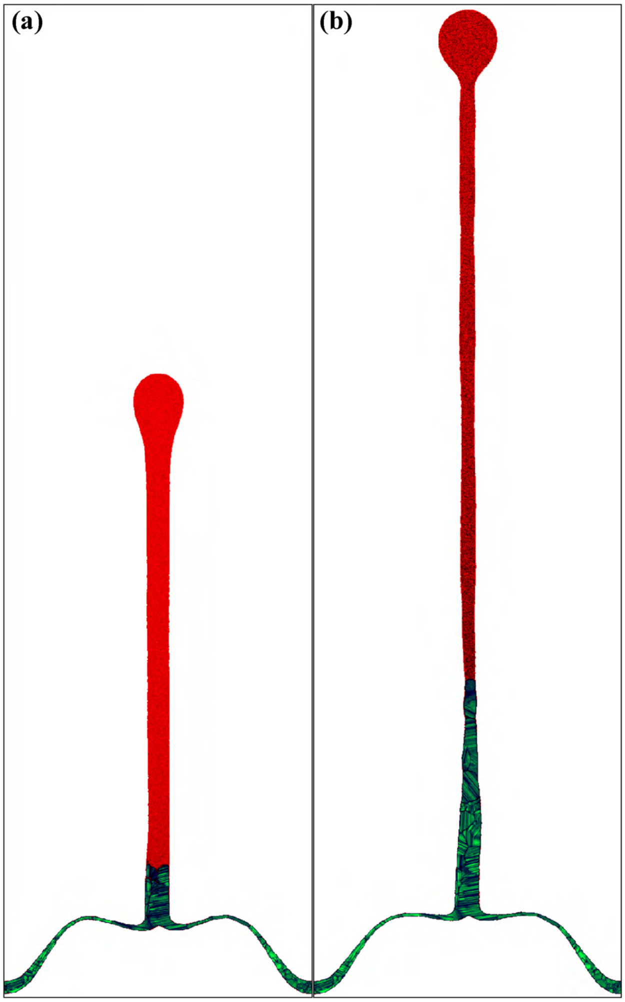

Fig. 8 Cross sections of sample from run 31+ listed in Table 2 and Fig. 6. The horizontal size of cross section is $L_b = 270\,\mathrm{nm}$. Formation of a very long jet accumulating most of mass from the circle $r < r_{\mathrm{cr}}$ defined in Fig. 1. The delayed freezing is one of the reasons leading to this superjets. At the equal heat diffusion coefficients, the freezing of jet is delayed as a result of the geometrical limitations. Indeed, the cooling thermal flux should pass (i) a long way through the jet, (ii) through the narrow neck, and (iii) along the very thinned film of the dome. **a** $t = 2.34\,\mathrm{ns}$, **b** $t = 4.536\,\mathrm{ns}$. The butt of jet with supercooled melt is recrystallized with high rate into polycrystalline solid composed with nano-sized grains

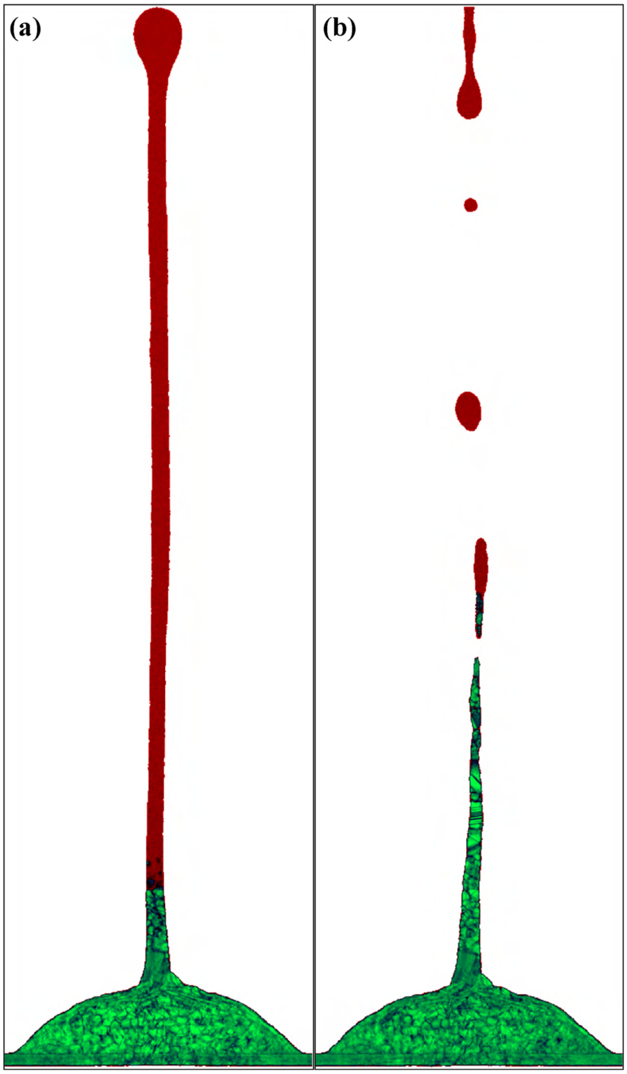

Fig. 9 Side-view of local atomic order parameter averaged along the view axis through the whole sample. The case 25+ from Table 2 and Fig. 6. We see how the jet gradually elongates with time while the lower part of the jet freezes. Small perturbations and the Rayleigh instability of jets lead to decay of the jet into the droplets. A chain of the droplets with varying size and velocities flies up. The largest and fastest one flies ahead. The decay tears off the droplet from the jet. Thus, a jet with the peaked tip is formed. These peaked jets are often seen in experiments at the enlarged pulse energies, see, e.g., Fig. No. 1(205 nJ) in [14] or Fig. No. 2(j) in [27]. Appearance of this peaked tip means that the droplets have been produced. In the another cases, the last nanodroplet from the chain may remain at the jet, then the jet with the frozen droplet at the tip will form. Thus, the cases with a droplet in the tip and with the peaked jet may alternate each other as energy of a laser pulse increases. **a** $t = 1.008\,\mathrm{ns}$, **b** $t = 2.232\,\mathrm{ns}$

explanation is based on the effect of surface tension acting like a spring returning a droplet.

Above, we have emphasized the similarity and difference between the runs 14 (Fig. 3) and 15 (Fig. 4). Let us compare the runs 15 and 11+ (Fig. 5) under the same angle. The pair 15, 11+ obviously differs from the run 14 since in the run 14 the bump keeps its integrity while in the both cases 15 and 11+ the shell of the dome is broken. But in the case 15 (Fig. 4), the breaking[3] takes place *after* the instant when the thickening turns back, while in the case 11+ (Fig. 5) the breaking takes place earlier—*before* this instant. Thus, in the run 11+ the ejecta flies out, while in the run 15 the ejecta forms the surface debris.

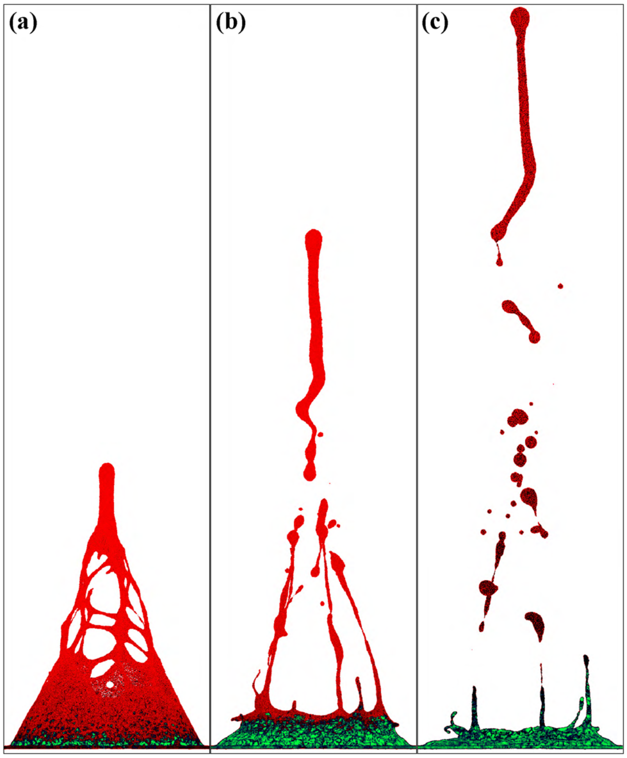

Fig. 10 Side-view of local atomic order parameter averaged along the view axis through the whole sample. The case 26+ is the case with significantly higher initial velocity $u_{\mathrm{cm}}(r = 0)$ relative to the cases 31+ and 25+ considered above, see Table 2 and Fig. 6. In this particular regime, the expansion and stretching are fast; therefore, the freezing has no time to freeze a dome, to achieve the base of the jet, and to begin to freeze the lower part of the jet. Only the lower part of the skirt of the dome is frozen to the instant when the breaking inside the liquid shell of the dome begins. The breaking of the liquid shell near the solid–liquid crystallization zone produces the family of the small capillary subjets shown in frame (**b**). Freezing of these small subjets results in formation of the nanocrown-like structures seen in frame (**c**). The nanocrowns have been observed in many experiments, see, e.g., Fig. No. 7 in [27], Fig. No. 2 in [28], and [29]. **a** $t = 144\,\mathrm{ps}$, **b** $t = 288\,\mathrm{ps}$, **c** $t = 432\,\mathrm{ps}$

4 Three-dimensional geometry

The 3D runs are listed in Table 2 and Fig. 6. Typical examples of thin 2-nm cross sections of samples are presented in Figs. 7 and 8, while Figs. 9 and 10 show side-

---

[3] The breaking is caused by strong thinning of a film, thanks to stretching.

views of whole samples. They demonstrate variety of regimes and sharp transitions between them. There are non-ejecting (they are blue in Fig. 6) and ejecting examples. The rather high initial speed non-ejecting case 30 in Table 2 and Fig. 6 is shown in Fig. 7. As we see, there is significant but moderate redistribution of mass along a film in the case 30, and there is the beginning of transformation of the thickening in the tip into the jet-like formation. Similar final shape with an elongated thickening appears in the case 23 with smaller relative initial speed. But small increase in the relative initial velocity qualitatively changes the situation—compare the runs 30 (Fig. 7) and 31 (Fig. 8).

Huge redistribution of mass takes place in all 3D ejecting cases listed in Table 2 and Fig. 6 (the red circles). Superlong jets are formed. Their maximum transient length is many times over the scale R_L. Thus, it is not easy to plot them in full length in our Figs. 3, 4, 5 and 7, 8, 9, 10 with the equivalent vertical and horizontal scales. In some cases, Figs. 5 and 9b, we need to cut the upper part of the droplet cloud. The lower part of the transient jet freezes as it takes place in the case 25+ shown in Fig. 9. While the upper part may either freeze as in the cases 30, 23, 20 or may decay into one, few, or many droplets as in Fig. 9b.

The rather long-lasting feed of a growing jet is the main reason of the strong elongation of a jet. Indeed, during the feed, the smaller and smaller vertical velocity is joined to the jet from the skirt of a film outside the axial region. Decrease in the inflowing velocity with time is caused by deceleration of motion of the dome, thanks to surface tension. Therefore, strong difference in velocities between the upper and the lower parts of a jet is formed. Namely, this difference gradually elongates the growing jet. The cross section of a jet becomes narrower as a result of this elongation. This narrowing of the cross section accompanies the decay of a liquid part of a jet into droplets as a result of the Rayleigh instability of a jet with a round cross section.

With the weakening of freezing rate, the regimes of expansion change from (i) the fully frozen nanobump (Fig. 7), the nanobump frozen with a jet and a droplet to (ii) the partially frozen jet (Fig. 9) and to (iii) the partially frozen dome (Fig. 10), where the dome filled with supercooled melt was recrystallized into polycrystalline solid film composed with nano-sized grains—see the similar phenomenon observed in [16]. Partial freezing of a jet or a dome enhances stretching of the remained liquid part because transfer into a solid strongly suppresses the stretchability of the solid part while velocity of a head of a liquid part keeps its value. Faster stretching means faster thinning of a jet or a film. Thinning in its turn brings the situation closer to the breaking.

The breaking is the reason for the ejecta formation. Tearing off a part of matter results in a structuring of the remained part like the formation of the peaked jets (Fig. 9b) or appearance of the frozen nanocrowns (Fig. 10c). As for the flying part of matter, we can say that a wide variety of ejecta regimes of the nanodroplets knockout takes place. A solitary droplet can fly away or a chain of the droplets flying one after other with a negligible angular spread may form an ejecta as in Fig. 9b. Transition from the solitary to the multiple cases are controlled by pulse energy. It is remarkable that such chains is observable in an accurate femtosecond laser experiments—see Fig. No. 3 (e–h) in paper [27]. The chain in paper [27] is produced by a *single* laser shot. It is necessary to cool down fast the liquid nanodroplets arriving to the receiver. This is necessary to freeze and keep the chain of droplets on a receiver in the form of the chain: the droplets are frozen together in line. For the purpose of the efficient heat removal from the molten droplets, a gold receiver (a gold film covering a silicate substrate) was used in work [27].

An angular distribution of the nanodroplets forming ejecta varies from very narrow to significantly wider distributions, compare the case shown in Fig. 9b and the cases in Figs. 5 d–f and 10c. Thus, the controlled deposition of ejecta into a small spot on a receiver is possible without a mask chipping out the rest of ejecta external relative to the desired spot (maskless technique). The deposition is regulated by an ejecta source created by a laser shot.

The droplets follow complicated evolution (with a large amplitude capillary oscillations and viscous dissipation) from the irregular shape to the round form under action of surface tension. In particular, long evolution takes place in the case of partially frozen dome like the dome shown in Fig. 10. The ejecta loses thermal contact with a cold part of a film. Thus, the nanodroplets in their flight cool down very slowly, thanks to low-power thermal radiation. The size/velocity distribution of droplets is sensitive to the details of a target and a laser shot. For example, the cutting of the jet from below by a breaking dome produces a giant fast first droplet which gradually forms from the separated jet in Fig. 10. The angular and size/velocity distributions depend also on the size R_L of an illuminated spot. The beautiful experiments and supporting simulations of the homogeneous case $R_L = \infty$ are presented in paper [30].

To conclude, it is worth to say that the 2T-HD and MD–MC codes are utilized to describe the different regimes of bulging. We found 3D cases where the strong thinning may happen with dome shell. The thinning is caused by the pumping-over of mass from the dome into an extra long jet.

Acknowledgments Authors thank RSCF (14-19-01599).

References

1. J. Bonse, A. Rosenfeld, J. Kruger, J. Appl. Phys. **106**, 104910 (2009)
2. M. Hashida, Y. Ikuta, Y. Miyasaka, S. Tokita, S. Sakabe, Appl. Phys. Lett. **102**, 174106 (2013)
3. O. Varlamova, J. Reif, S. Varlamov, M. Bestehorn, ch. 1 in *Progress in Nonlinear Nano-Optics*, ed. by S. Sakabe, C. Lienau, R. Grunwald (Springer Int. Publ., 2015)
4. J.-M. Savolainen, M.S. Christensen, P. Balling, Phys. Rev. B **84**, 193410 (2011)
5. E.L. Gurevich, Phys. Rev. E **83**, 031604 (2011)
6. A.A. Ionin, S.I. Kudryashov, S.V. Makarov et al., Laser Phys. Lett. **10**, 056004 (2013)
7. S.I. Ashitkov, S.A. Romashevskii, P.S. Komarov, A.A. Burmistrov, V.V. Zhakhovskii, N.A. Inogamov, M.B. Agranat, Quantum Electron. **45**(6), 547 (2015)
8. C. Wu, M.S. Christensen, J.-M. Savolainen, P. Balling, L.V. Zhigilei, Phys. Rev. B **91**, 035413 (2015)
9. N.A. Inogamov, V.V. Zhakhovsky, V.A. Khokhlov, S.I. Ashitkov, Y.N. Emirov, K.V. Khichshenko, A.Y. Faenov, T.A. Pikuz, M. Ishino, M. Kando, N. Hasegawa, M. Nishikino, P.S. Komarov, B.J. Demaske, M.B. Agranat, S.I. Anisimov, T. Kawachi, I.I. Oleynik, J. Phys. Conf. Ser. **510**, 012041 (2014)
10. Y. Nakata, T. Okada, M. Maeda, Jpn. J. Appl. Phys. **42**, L1452 (2003)
11. F. Korte, J. Koch, B.N. Chichkov, Appl. Phys. A **79**, 879 (2004)
12. Y. Nakata, T. Hiromoto, N. Miyanaga, Appl. Phys. A **101**, 471 (2010)
13. C. Unger, J. Koch, L. Overmeyer, B.N. Chichkov, Opt. Express **20**(22), 24864 (2012)
14. D. Wortmann, J. Koch, M. Reininghaus, C. Unger, C. Hulverscheidt, D. Ivanov, B.N. Chichkov, J. Laser Appl. **24**, 042017 (2012)
15. Y.P. Meshcheryakov, M.V. Shugaev, T. Mattle, T. Lippert, N.M. Bulgakova, Appl. Phys. A **113**(2), 521 (2013)
16. D.S. Ivanov, A.I. Kuznetsov, V.P. Lipp, B. Rethfeld, B.N. Chichkov, M.E. Garcia, W. Schulz, Appl. Phys. A **111**(3), 675 (2013)
17. S.V. Starikov, V.V. Pisarev, J. Appl. Phys. **117**, 135901 (2015)
18. N.A. Inogamov, V.V. Zhakhovskii, V.A. Khokhlov, J. Exp. Theor. Phys. (JETP) **120**(1), 15 (2015)
19. M.A. Gubko, W. Husinsky, A.A. Ionin, S.I. Kudryashov, S.V. Makarov, C.R. Nathala, A.A. Rudenko, L.V. Seleznev, D.V. Sinitsyn, I.V. Treshin, Laser Phys. Lett. **11**, 065301 (2014)
20. D.A. Zayarny, A.A. Ionin, S.I. Kudryashov, S.V. Makarov, A.A. Rudenko, S.G. Bezhanov, S.A. Uryupin, A.P. Kanavin, V.I. Emelyanov, S.V. Alferov, S.N. Khonina, S.V. Karpeev, A.A. Kuchmizhak, O.B. Vitrik, Y.N. Kulchin, JETP Lett. **101**(6), 394–397 (2015)
21. V. Zhakhovskii, K. Nishihara, Y. Fukuda, S. Shimojo, T. Akiyama, S. Miyanaga, H. Sone, H. Kobayashi, E. Ito, Y. Seo, M. Tamura, Y. Ueshima, A new dynamical domain decomposition method for parallel molecular dynamics simulation, in *IEEE Proceeding of the 5th International Symposium on Cluster Computing and Grid (CCGrid 2005)*, vol. 2, May 9–12, 2005, (Cardiff, UK, 2005), pp. 848–854
22. V.K. Semenchenko, *Surface Phenomena in Metals and Alloys* (Pergamon, New York, 1961)
23. V.V. Zhakhovskii, N.A. Inogamov, Y.V. Petrov, S.I. Ashitkov, K. Nishihara, Appl. Surf. Sci. **255**, 9592 (2009)
24. V.I. Emel'yanov, D.A. Zayarniy, A.A. Ionin, I.V. Kiseleva, S.I. Kudryashov, S.V. Makarov, T.H.T. Nguyen, A.A. Rudenko, JETP Lett. **99**(9), 518–522 (2014)
25. A.I. Kuznetsov, J. Koch, B.N. Chichkov, Appl. Phys. A **94**, 221–230 (2009)
26. P.A. Danilov, E.A. Drozdova, A.A. Ionin, S.I. Kudryashov, S.B. Odinokov, A.A. Rudenko, V.I. Yurovskikh, D.A. Zayarny, Appl. Phys. A **117**, 981–985 (2014)
27. A.I. Kuznetsov, C. Unger, J. Koch, B.N. Chichkov, Appl. Phys. A **106**, 479–487 (2012)
28. Y. Nakata, K. Tsuchida, N. Miyanaga, T. Okada, J. Laser Micro Nanoeng. (JLMN) **3**(2), 63–66 (2008)
29. Y.N. Kulchin, O.B. Vitrik, A.A. Kuchmizhak, V.I. Emelyanov, A.A. Ionin, S.I. Kudryashov, S.V. Makarov, Phys. Rev. E **90**, 023017 (2014)
30. C.M. Rouleau, C.-Y. Shih, C. Wu, L.V. Zhigilei, A.A. Puretzky, D.B. Geohegan, Appl. Phys. Lett. **104**, 193106 (2014)